3 Simulation of CLEO II and CLEO III

The initial comparison of various concepts for the inner detector was accomplished using programs which contain parametric models of the detector performance for single charged tracks. We examined at the resolutions for tracking variables as a function of momentum and angle for each candidate detector and compared them with a similar model of the existing CLEO II detector. These studies gave the quick and reliable feedback necessary to optimize the conceptual design. In addition, this study identified potential problem areas to be addressed in a more complete simulation.

Once the rough design of the detector was specified by the track parameter studies, a full Monte Carlo simulation of the tracking system was performed. The simulation used the CLEO track reconstruction code DUET. It deposited ionization in each device, smeared the ionization, added noise, introduced multiple scattering from all the material traversed including the gas and discrete wires, and removed hits according to an efficiency table. The tracking code was then asked to do the pattern recognition to find the appropriate hits on each track and then reconstruct the track parameters by fitting those hits. This code was used to measure the single track parameters and to measure the resolution and reconstruction efficiency for physics quantities of simulated B decays. Using this code we were able to reproduce the present CLEO II track parameter and mass resolutions and compare them with the CLEO III model.

3.1 Parametric model studies

The CLEO III upgrade is primarily driven by the desire to study rare B decays. Operationally, this means providing space for particle identification by reducing the tracking length relative to CLEO II while maintaining the tracking performance by simultaneously reducing the amount of material. The material in the various devices of CLEO II which a charged particle under normal incidence traverses, is listed in Table 10. The CLEO III design was arrived at by studying the effects of changes to the inner detector geometry and material on the track parameters: $\mathrm{d}p/p$, $\sigma_{\tan\theta}$, σ_{IP}, σ_z, and σ_ϕ. All designs were compared with a similar model for CLEO II. In these studies, the various tracking layers were defined by their radii and intrinsic spatial resolution, multiple scattering was added at discrete radii, and the track parameter resolutions for a given momentum and angle were derived by a matrix inversion technique. The designs studied were constructed out of modular pieces consistent with the new IR. The cell design for the tracking chambers was based on that used in the CLEO II drift chamber. The modular pieces for the parametric model were chosen among the specifications shown in Table 11.

The track parameter studies showed that only two tracking devices are necessary, an inner silicon detector followed by a large, uninterrupted, low mass drift chamber. Both the silicon and the inner section of the drift chamber will follow the stepped structure of the

Table 10: Material in the CLEO II inner detector at normal incidence.

Subsystem	Material (% X_0)
Beam Pipe	0.44
PTL	0.40
VD	0.94
DR	
- inner wall/cathode	0.77
- gas	0.43
- wires	0.32
- endplates and electronics	60–100
Silicon†	
- detectors	0.4/layer
- outer support	0.10

† This three layer, double-sided detector will replace the PTL in 1994.

Table 11: Definitions of devices used in the track parameter study.

Subsystem	$r\phi$ resolution	z resolution	Material
Si	15 μm	30 μm	0.40%/layer
Tube Detector	50 μm	—	0.06%/layer
VD	100 μm	—	variable
DR wires	150 μm	3–5mm (stereo)	variable
DR cathodes		1.8mm	

machine around a 300 mrad line to achieve an active detector region beginning at 330 mrad. The minimum achievable drift chamber radius is set to be 17.5 cm by the radius of the accelerator rare-earth, permanent quadrupole. The maximum drift chamber radius is set at 82 cm to allow 20 cm of space for the particle identification system.

The critical parameter for achieving the best momentum resolution in every design was found to be the uninterrupted length of the drift chamber; *i.e.,* with the outer radius determined, the inner edge should extend to the smallest radius without encountering any walls or additional material. In the CLEO III design all walls and/or material between the silicon and the drift chamber have been reduced to the equivalent of one 0.5 mm beryllium layer. Furthermore, a drift chamber gas with twice the radiation length of argon-ethane ($X_0 = 166$ m for Ar-ethane) is needed to maintain the tracking resolution equal to that of CLEO II. We note that under these circumstances the addition of any tracking chamber between the silicon and drift chamber degrades the performance of the detector.

The silicon detector begins immediately after the beam pipe which is chosen by background considerations to have a radius of 2.2 cm. The detector has four layers at the approximate radii of 2.5 cm, 3.75 cm, 7.5 cm, and 10.0 cm. The very high resolution of a silicon detector compared to a wire chamber leads to a separated function detector. Namely, the silicon measures the impact parameter in z and polar angle whereas the drift chamber measures curvature. Both devices contribute to measuring the impact parameter in $r\phi$ and the azimuthal angle.

As stated earlier, the mark of a successful design is that it at least reproduce the current CLEO II tracking system performance. In Table 12 we show the five track parameters generated by the parametric studies for the CLEO II detector, the CLEO II/Si detector in which the PTL is replaced with a 3 layer silicon detector, and the proposed CLEO III detector. **For every parameter and at all momenta the CLEO III design is comparable to or better than the previous detectors.**

The CLEO III design described above has the added benefit that by moving the outer radial edge of the drift chamber to smaller radius, the solid angle of "good barrel" crystals increases from 70% to 77% of 4π. This has the effect of deemphasizing the importance of the endcaps.

We note that increasing the magnetic field above 1.5 Tesla would also improve the tracking as would an improvement in the spatial resolution of the tracking chambers. There is no mechanism, however, for increasing the CLEO magnetic field and there is no obvious technology that would allow a significant improvement in drift chamber spatial resolution technology beyond the present DR 2, so we have not pursued these possibilities. We also note that the CLEO III design is especially sensitive to the placement of the material: the addition of 0.5% X_0 at $r = 30$ cm has the effect of deteriorating the tracking by an amount equivalent to placing 2.5% X_0 at $r = 17.5$ cm. Care in placement of material is also important for the energy resolution and efficiency of the crystal calorimeter.

Table 12: Results of the track parameter studies at 90° for CLEO II, CLEO II with the 1994 silicon detector, and CLEO III.

		p (GeV/c)				
	Detector	0.25	0.50	1.0	2.0	5.0
dp/p^2 (%/GeV/c)						
	CLEO II	1.10	0.58	0.32	0.20	0.13
	CLEO II/Si	1.10	0.58	0.32	0.20	0.13
	CLEO III	0.98	0.54	0.31	0.20	0.13
$\sigma_{\tan\theta}$ (10^{-3})						
	CLEO II	6.6	3.7	2.4	1.9	1.8
	CLEO II/Si	4.8	3.7	1.7	1.2	1.0
	CLEO III	4.7	2.5	1.3	0.7	0.5
σ_{IP} (μm)						
	CLEO II	166	102	64	42	30
	CLEO II/Si	101	57	35	22	14
	CLEO III	105	58	34	21	14
σ_z (μm)						
	CLEO II	944	783	733	720	716
	CLEO II/Si	116	74	53	43	39
	CLEO III	117	67	43	33	30

Table 13: Simulated reconstruction efficiency and mass resolution for 250 MeV/c π^0's generated with $|\cos\theta| < 0.7$ where both photons are within $|\cos\theta| < 0.7$. The radiation lengths are for 90° and include all material in front of the CsI crystals. The reconstruction efficiency is relative to that for the calorimeter with no material other than its support container—the absolute reconstruction efficiency in this case is 68%.

Configuration	PID (% X_0)	Total (% X_0)	Recon. eff. (%)	$\sigma_{m_{\pi^0}}$ (MeV/c^2)
CsI container	—	1.8	100	4.2±0.1
CLEO III w/ aerogel	5.0	13.0	88±2	4.2±0.1
CLEO III w/ RICH	8.0	16.0	85±2	4.3±0.1
CLEO III w/ high pressure tubes	9.0	17.0	84±2	4.2±0.1
CLEO II w/ TOF scintillator	12.4	20.4	81±2	4.5±0.1

3.2 Material effects on the CsI calorimeter

In Table 13 we show the results of a GEANT simulation of the effects of material in front of the barrel crystal calorimeter for CLEO II and for various CLEO III configurations. For this simulation the π^0's were generated uniformly in $|\cos\theta| < 0.7$ (θ between 45 and 135°) with a momentum of 250 MeV/c. Both photons were required to be detected in the good barrel region. The material of the particle identification systems was distributed as might occur in an actual implementation. The radiation lengths are representative and might differ slightly in a constructed detector. The results of this simulation indicate a linear loss of efficiency even for small amounts of material and an indication of loss of π^0 mass resolution when more than 0.2 X_0 is traversed. In Fig. 21 we show the π^0 mass resolution attained in the CLEO II detector when one photon is constrained to the good barrel region and the other passes through varying material radiation thicknesses. A striking degradation of the mass resolution from 5 to 12 MeV/c^2 can be observed. This work indicates that in the central region the total amount of material in front of the calorimeter should be kept below 20% X_0 in order to maintain the calorimeter performance relative to CLEO II. It also indicates a need to reduce the amount of material in the barrel/endcap transition region and in front of the endcaps.

3.3 Simulation results

The parametric tracking study described above provided a means for rapidly prototyping various CLEO III tracking configurations and comparing them with the corresponding parametric model of CLEO II. Once an optimum was achieved, the configuration was fully simulated using standard CLEO Monte Carlo and reconstruction codes. The results presented below are for Monte Carlo generated events reconstructed with the CLEO II track

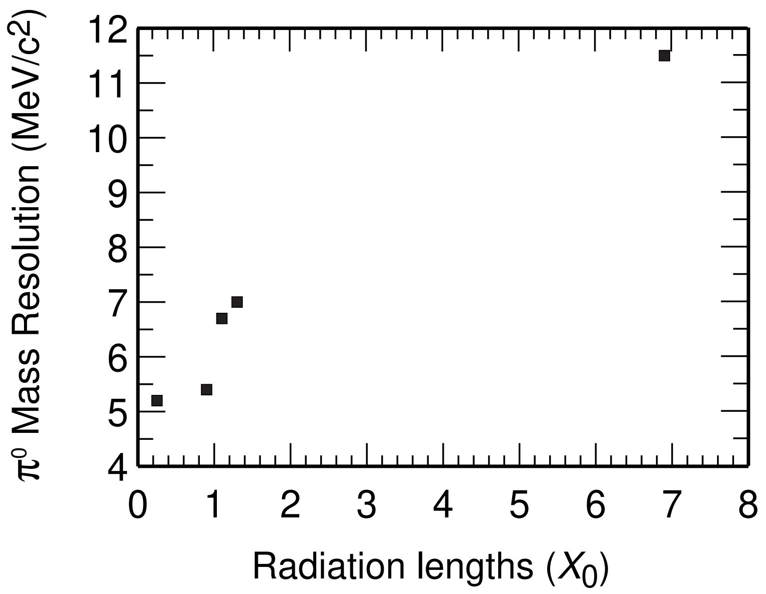

Figure 21: The CLEO II measured mass resolution for π^0's as a function of material traversed by one photon when the second photon is required to be in the good barrel region, $|\cos\theta| < 0.7$. The points around 1 X_0 are in the endcap region and the point around 7 X_0 occurs at eight discrete ϕ locations at the outer edge of the drift chamber endplates where the support system for the CESR quadrupoles is attached.

finding code, DUET, and with a version modified to include silicon for the CLEO III tracking system. The algorithms used in the track finding code were identical for the CLEO II and CLEO III detectors. This may not be optimum for CLEO III track reconstruction but was used as a basis for comparison. The position of the drift chamber layers for CLEO III were chosen to be identical to CLEO II. The smaller outer radius of the drift chamber was simulated by removing the appropriate number of CLEO II layers. Once again this choice may not be optimum for CLEO III but was used as a reference.

3.3.1 Single track simulations

In order to study the effects of track reconstruction on the various track parameters, ten thousand single charged pion events were generated isotropically over the solid angle for each of several momenta. The performances versus momentum for CLEO II and CLEO III are shown in Figs. 22, 23, and 24 for momentum resolution, z resolution, and $\tan\theta$ resolution, respectively. These Monte Carlo results reproduce those obtained in CLEO II data and confirm what was indicated in Table 12, namely that the new detector is comparable to CLEO II everywhere except at low momentum where it is noticeably better, primarily since there is less material in the tracking path.

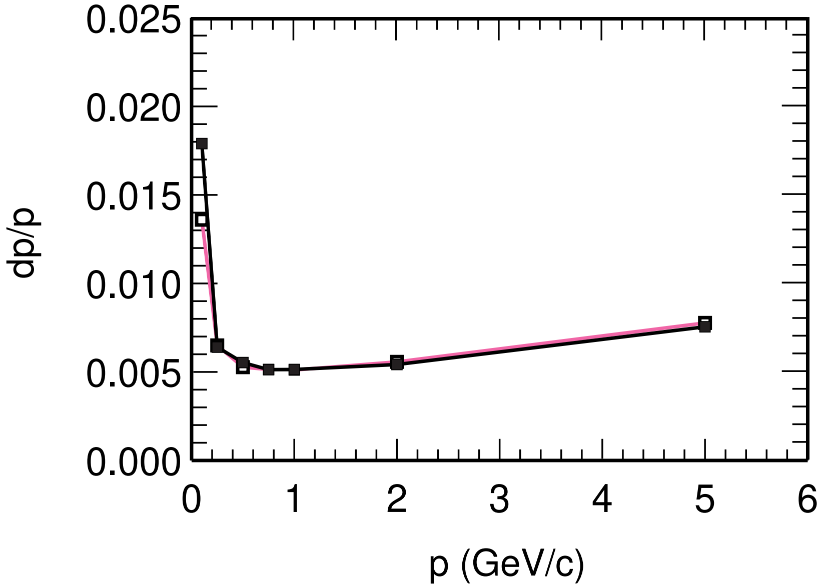

Figure 22: The momentum resolution determined from the Monte Carlo simulation for CLEO II (solid squares) and CLEO III (open squares).

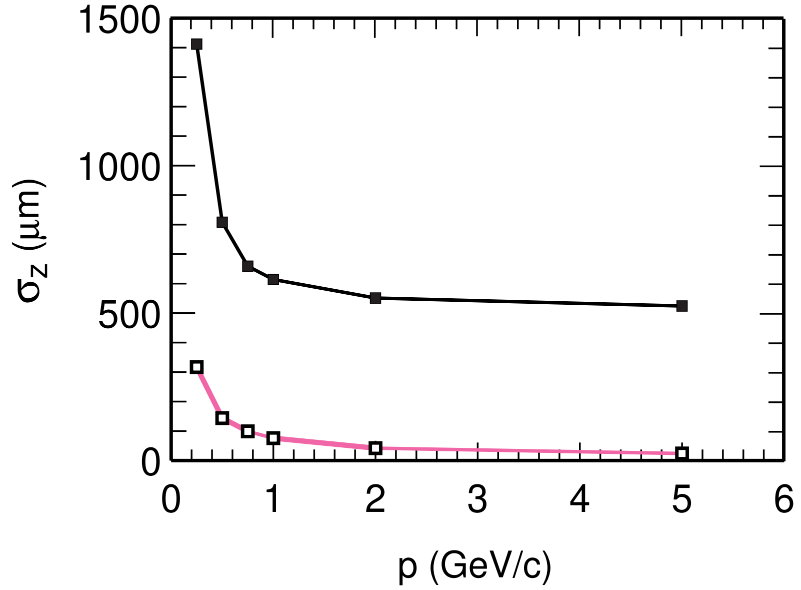

Figure 23: Comparison of z resolution determined from the Monte Carlo simulation for CLEO II (solid squares) and CLEO III (open squares).

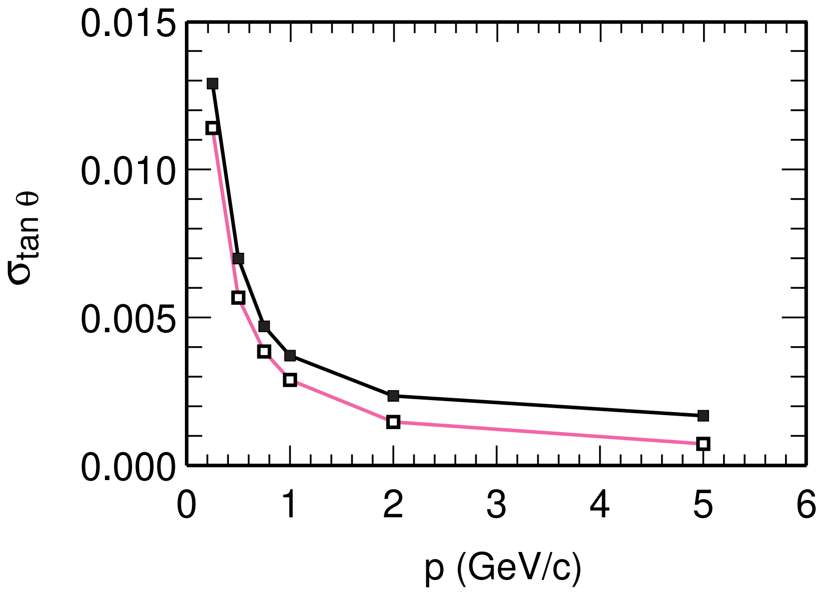

Figure 24: Comparison of $\tan\theta$ resolution determined from the Monte Carlo simulation for CLEO II (solid squares) and CLEO III (open squares).

3.3.2 $D^* - D$ mass difference

As a more stringent test we have studied physics processes involving mass reconstruction using algorithms and code that are presently used in CLEO II. Ten thousand D^* events with the decay $D^* \to D^0\pi$ followed by $D^0 \to K\pi$ were generated isotropically in $\cos\theta$. In Fig. 25 we show the $D^* - D^0$ mass difference, $\Delta m = m_{K\pi\pi} - m_{K\pi}$, as a function of D^* momentum. A cut on this mass difference is a common method used to tag D^0's in the CLEO II detector. Over the entire momentum range the new detector is comparable or better than CLEO II. This can be attributed to two effects, the superior momentum resolution and the superior angular resolution of CLEO III. We note that the CLEO III detector reaches $\sigma_{\Delta m} = 0.7$ MeV/c^2 at $p_{D^*} = 2$ GeV/c^2 and by more appropriate use of the silicon this might be reduced to 0.6 MeV/c^2.

3.3.3 B decay simulations

Before finalizing the design, more detailed simulations of the detector capabilities were undertaken. In particular, the performance of the detector for specific physics modes was studied in detail. These processes described below reflect some of the important physics goals of CLEO III and were chosen in such a way as to test the performance of the detector for a wide range of physics. For each process, $e^+e^- \to B\bar{B}$ was simulated with one B forced to decay in a particular fashion while the other decayed according to the B branching ratios. Thus all track overlap, lost track, multiplicity, and combinatoric problems were present.

Presently CLEO II has a large program to reconstruct charged and neutral B decays

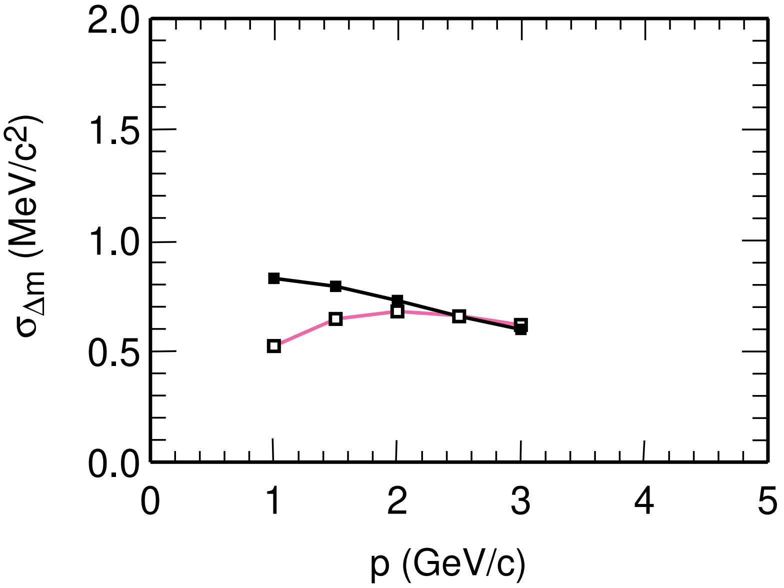

Figure 25: The $D^* - D^0$ mass difference resolution as a function of D^* momentum determined from the Monte Carlo simulation for CLEO II (solid squares) and CLEO III (open squares).

via the mode $D^*\pi$. In this analysis, two variables are plotted: the $D^* - D^0$ mass difference and the D^0 mass. After cutting on these variables, a beam energy constraint is applied to determine the candidate B mass: $m_B = \sqrt{E_{beam}^2 - (\Sigma p_i)^2}$. In Fig. 26 we show the $D^* - D^0$ mass difference for D^*'s from the B decay $B^0 \to D^*\pi$. The resolution is comparable in CLEO II and CLEO III. This is also true for the D^0 mass shown in Fig. 26 where the D^0 has been reconstructed through its $K\pi$ mode.

As another example, we consider the rare B decay $B^+ \to D^0 K^+$ where the D^0 then decays to K^+K^-. This is an interesting decay since it may be used to observe CP violation in a symmetric machine environment. In Fig. 27 we show the reconstructed D^0 mass and in Fig. 27 we show ΔE, the energy difference between the beam energy and the sum of the D^0 and K energies. Again, comparable performance for CLEO III relative to CLEO II has been achieved.

As yet another example we consider the rare B decay $B^0 \to \pi^+\pi^-$. In Fig. 28 we show the reconstructed $\pi\pi$ mass resolution for CLEO II and CLEO III. In Fig. 28 we also show the difference between the beam energy and the total energy of the two pions and the B mass for a constrained fit using the beam energy and the reconstructed π momenta. Again, comparable performance to CLEO II has been maintained.

In Table 14 we present a summary of the results obtained in the physics simulations as shown in Figs. 26-28. Over a wide range of physics modes, the CLEO III detector maintains the excellent performance of CLEO II. As stated earlier, additional gains may be made by using CLEO III specific tracking reconstruction code and by more appropriate placement of the tracking layers. This work in presently underway.

Table 14: A summary of the comparison of tracking simulations for CLEO II and CLEO III for the benchmark processes $B \to D^*\pi$, $B \to D^0 K$, and $B \to \pi^+\pi^-$. The resolutions are the standard deviations of fits to the individual plots in Figs. 26-28.

Process	Measurement	CLEO II resolution	CLEO III resolution
$B \to D^*\pi$			
$D^* \to D^0\pi$	$m_{D^*} - m_D$ (MeV/c^2)	0.48±0.02	0.42±0.02
$D^0 \to K\pi$	$m_{K\pi}$ (MeV/c^2)	6.31±0.28	6.07±0.25
$B \to DK$			
$D \to K^+K^-$	$E_{beam} - E_B$ (MeV)	16.1±0.3	17.0±0.3
	$m_{K^+K^-}$ (MeV/c^2)	5.59±0.13	5.62±0.12
$B \to \pi^+\pi^-$			
	$m_{\pi^+\pi^-}$ (MeV/c^2)	20.9±0.4	21.3±0.4
	$m_{\pi^+\pi^-}$ constrained	2.40±0.03	2.38±0.03
	$E_{beam} - E_B$ (MeV)	20.9±0.3	22.1±0.3

3.4 Summary

The physics modes investigated test virtually every aspect of the proposed detector. It is hard to imagine that other processes will require physics capabilities not covered in one of the above modes. Our wealth of experience in using CLEO II for all aspects of b, c, and τ physics together with our detailed simulation of the CLEO III detector give us great confidence that the new detector is optimally matched to our physics goals.

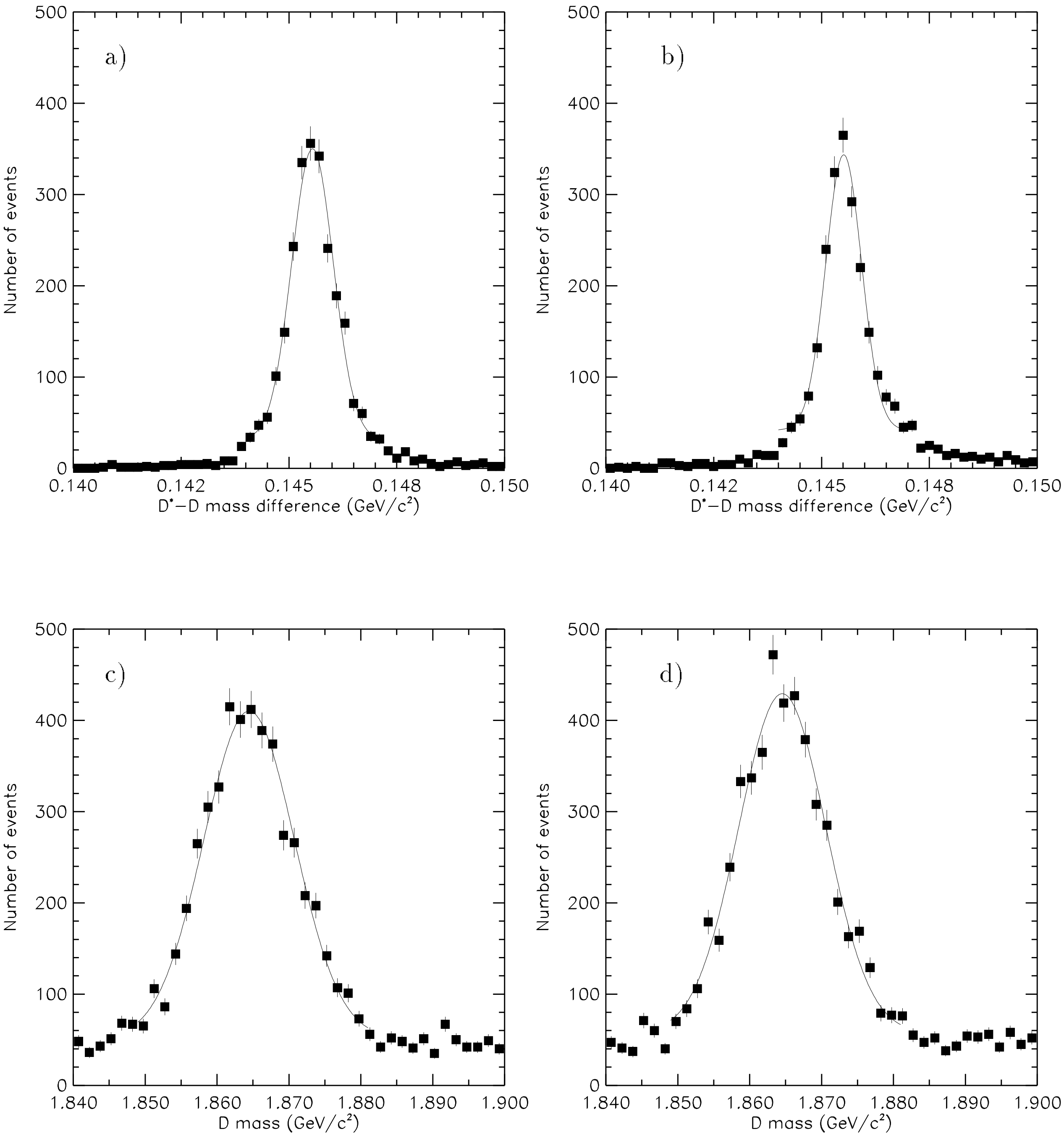

Figure 26: For the decay chain $B \to D^*\pi$, $D^* \to D^0\pi$, $D^0 \to K\pi$, the reconstructed D^0 mass is shown for a) CLEO II and b) CLEO III and the $D^* - D^0$ mass difference is shown for c) CLEO II and d) CLEO III. The solid lines are fits to a gaussian and a flat background.

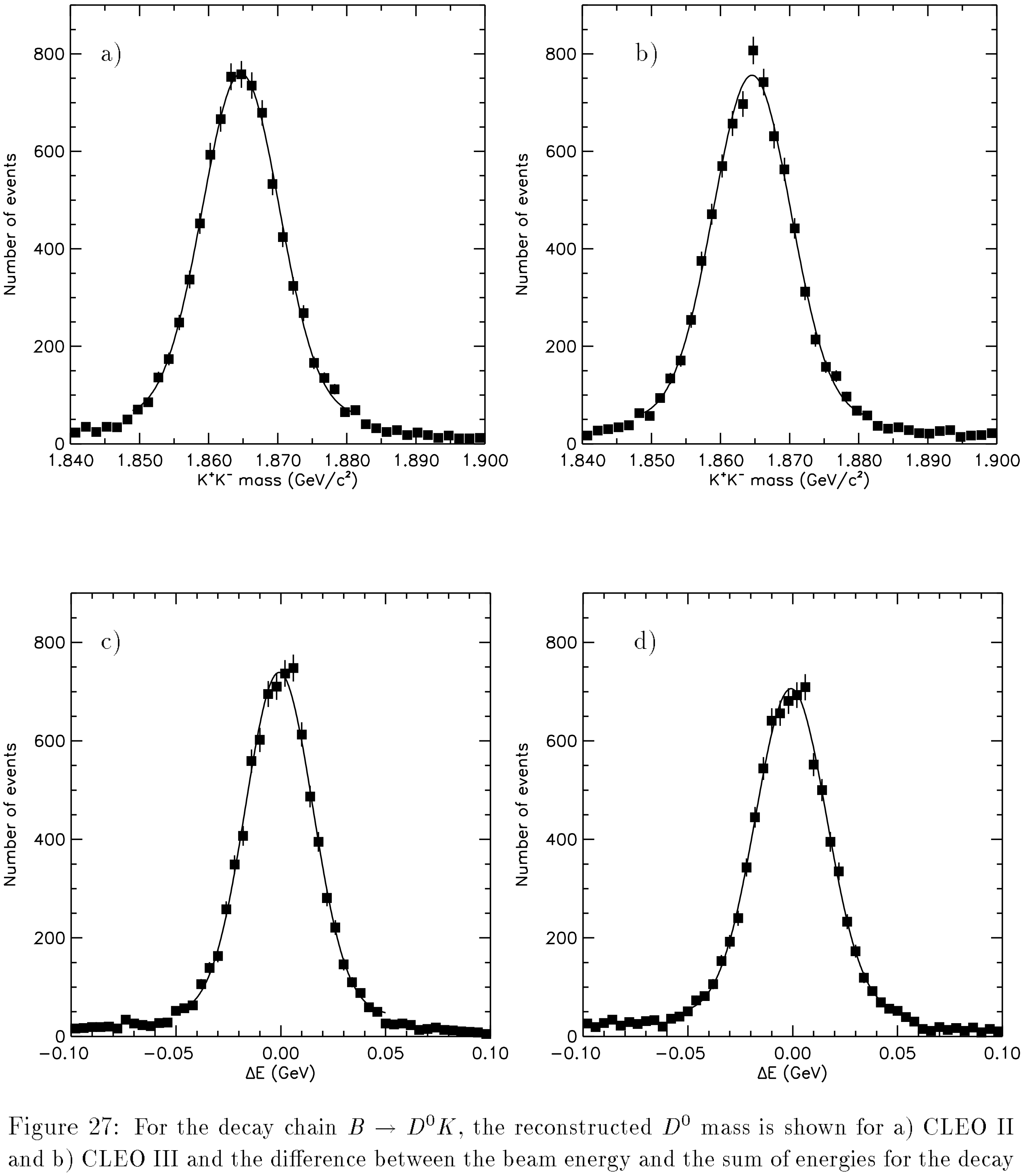

Figure 27: For the decay chain $B \to D^0 K$, the reconstructed D^0 mass is shown for a) CLEO II and b) CLEO III and the difference between the beam energy and the sum of energies for the decay products is shown for c) CLEO II and d) CLEO III. The solid lines are fits to a gaussian and a flat background.

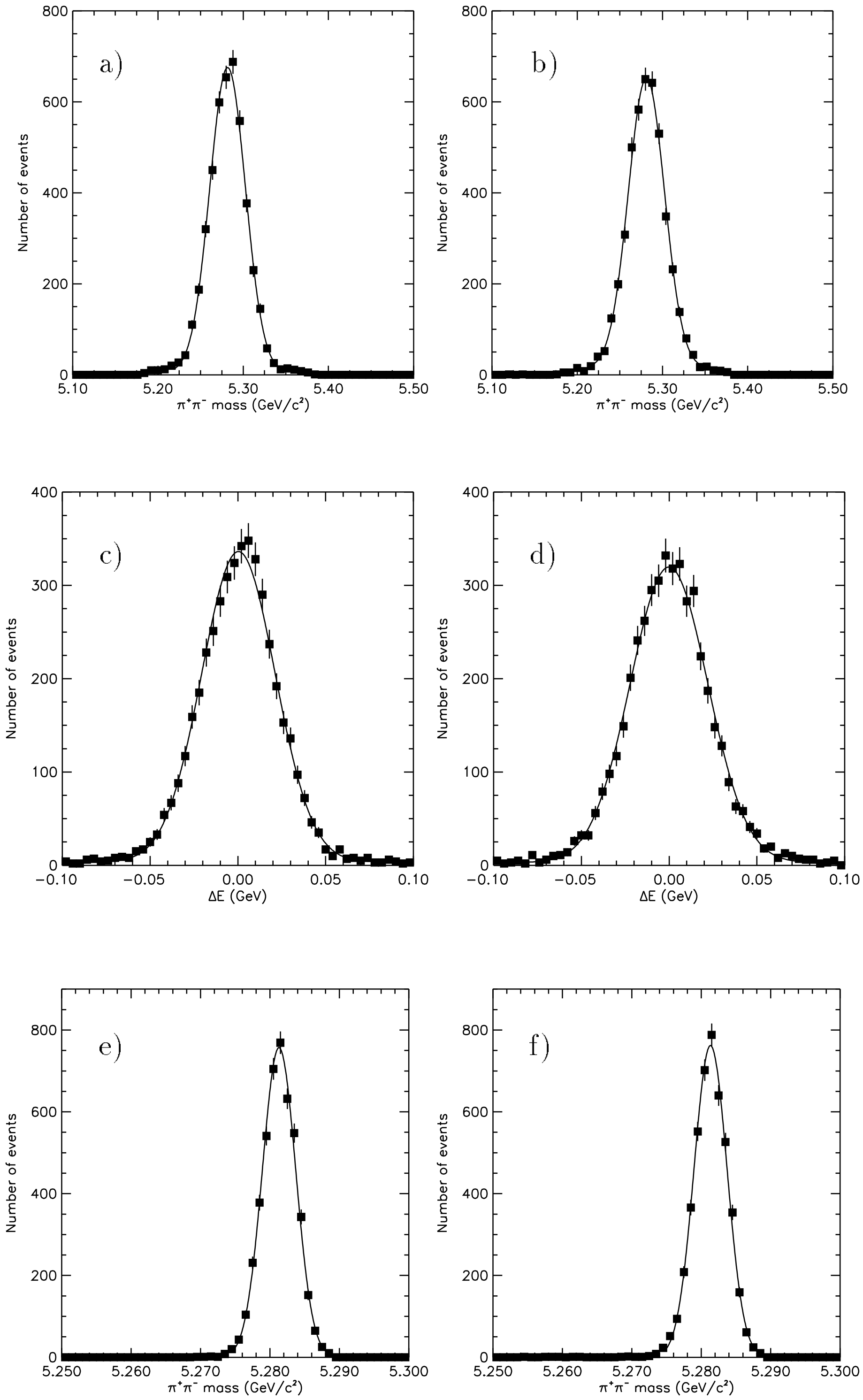

Figure 28: For $B \to \pi^+\pi^-$, the reconstructed $\pi\pi$ mass is shown for a) CLEO II and b) CLEO III, the difference between the beam energy and the total energy of the two π's is show for c) CLEO II and d) CLEO III, and the $\pi\pi$ mass reconstructed with a beam energy constraint applied is shown for e) CLEO II and f) CLEO III. The solid lines are fits to a gaussian and a flat background.